BIOCHEMISTRY

Long-range allosteric signaling in red light–regulated diguanylyl cyclases

Geoffrey Gourinchas,[1] Stefan Etzl,[1] Christoph Göbl,[2,3] Uršula Vide,[1] Tobias Madl,[2,3,4] Andreas Winkler[1]*

Nature has evolved an astonishingly modular architecture of covalently linked protein domains with diverse functionalities to enable complex cellular networks that are critical for cell survival. The coupling of sensory modules with enzymatic effectors allows direct allosteric regulation of cellular signaling molecules in response to diverse stimuli. We present molecular details of red light–sensing bacteriophytochromes linked to cyclic dimeric guanosine monophosphate–producing diguanylyl cyclases. Elucidation of the first crystal structure of a full-length phytochrome with its enzymatic effector, in combination with the characterization of light-induced changes in conformational dynamics, reveals how allosteric light regulation is fine-tuned by the architecture and composition of the coiled-coil sensor-effector linker and also the central helical spine. We anticipate that consideration of molecular principles of sensor-effector coupling, going beyond the length of the characteristic linker, and the appreciation of dynamically driven allostery will open up new directions for the design of novel red light–regulated optogenetic tools.

INTRODUCTION

During evolution, nature has developed a remarkably modular architecture of covalently linked protein domains. Combining individual building blocks from an array of diverse functionalities enabled organisms to develop complex cellular networks that are critical for homeostasis. The frequently observed coupling of sensory modules with enzymatic effectors enables direct allosteric regulation of, for example, second messenger levels in response to diverse stimuli. Recently, light-regulated enzymes have attracted special attention because of their potential for optogenetic applications (1). However, naturally occurring sensor-effector couples are limited, and our current understanding of molecular mechanisms underlying their modularity prevents the rational design of efficient, novel sensor-effector combinations. Optogenetic platforms based on near-infrared light photoreceptors have recently attracted special attention because of their potential for deep tissue stimulation in mammalian systems (2, 3). Most of these optogenetic tools are based on natural, noncovalent interactions of plant phytochromes with transcription factors, which can be adapted to a variety of cellular targets [reviewed by Tischer and Weiner (1)]. In contrast, the design of novel tools for direct allosteric control of enzymatic activity appears more complex because of a limited understanding of molecular mechanisms involved in signal transduction between sensor and effector domains. Nevertheless, bacterial phytochromes have been successfully used for the generation of artificial red light–regulated adenylyl cyclases (4) and phosphodiesterases (5). However, establishing tools for direct manipulation of enzymatic activities still requires substantial screening efforts, and concepts learned from successful designs are not easily transferable even to closely related systems. Especially the lack of structural information for natural or ar-

tificial full-length phytochromes precludes the functional interpretation of linker elements that covalently tether sensor to effector.

To overcome this limitation, we focused on naturally occurring systems that allow red light regulation of the bacterial second messenger bis-(3′-5′)-cyclic dimeric guanosine monophosphate (c-di-GMP) (6) by linking canonical bacteriophytochromes (7) with GGDEF domains (8) featuring diguanylyl cyclase (DGC) activity [phytochrome-activated diguanylyl cyclase (PadC)]. Although related systems have been characterized previously (9–11), we concentrated on natural variants that feature a defined PAS-GAF-PHY-GGDEF domain architecture (Fig. 1A) and initially characterized three constructs belonging to subgroups with characteristic linker length variations between the PHY and GGDEF domains. The systematic differences of one or two heptad repeats support the relevance of a coiled-coil structure preceding the DGC (fig. S1). This structural element is also observed in other sensor DGCs (12, 13) and is functionally relevant for GGDEF regulation (14, 15). However, molecular details of the structural changes induced by the reversible photoswitching of the phytochrome sensor between its dark-state conformation (P_r) and its red light–activated P_{fr} form with respect to long-range signaling to effector domains are not well understood.

Here, we describe the first full-length crystal structure of a bacteriophytochrome in its P_r state linked to its functional, enzymatic output, revealing a parallel dimeric arrangement of the sensor and effector domains. This structure provides a foundation for increasing our understanding of the fine-tuned coupling mechanism of phytochrome sensors with various effector domains. The characterization of in-solution conformational dynamics substantiates the involvement of previously proposed functionally relevant structural elements observed in phytochromes (10, 16, 17) and highlights their dynamic interplay with the coiled-coil sensor-effector linker region. Our results demonstrate how allosteric light regulation of enzymatic effectors is fine-tuned by the architecture and composition of the coiled-coil linker and by the central helical spine of phytochromes without direct interaction of the sensory module. We anticipate that consideration of molecular principles of sensor-effector coupling, going beyond the length of the characteristic linker, will open up new directions for the design of novel red light–regulated optogenetic tools.

[1]Institute of Biochemistry, Graz University of Technology, Petersgasse 12/II, 8010 Graz, Austria. [2]Center for Integrated Protein Science Munich, Technische Universität München, Department of Chemistry, Lichtenbergstraße 4, 85748 Garching, Germany. [3]Institute of Structural Biology, Helmholtz Zentrum München, Ingolstädter Landstraße 1, 85764 Neuherberg, Germany. [4]Institute of Molecular Biology and Biochemistry, Medical University of Graz, Harrachgasse 21/III, 8010 Graz, Austria.
*Corresponding author. Email: andreas.winkler@tugraz.at

RESULTS

Structure of a full-length red light–activated DGC

We characterized three naturally occurring PadC homologs with different linker length between their PHY and DGC domains. All constructs feature a characteristic bacteriophytochrome photocycle (Fig. 1B, Table 1, and fig. S2, A and B) and light-regulated conversion of two molecules of guanosine triphosphate (GTP) to c-di-GMP (Fig. 1C and fig. S2, C and D). Because PadC from *Idiomarina* sp. A28L (*Is*PadC) showed the highest dynamic range of c-di-GMP formation, we focused on this construct for a more detailed biophysical characterization.

We crystallized full-length *Is*PadC under dark conditions and also obtained a GTP-bound complex from soaking experiments. In addition, a truncated version of *Is*PadC corresponding to the photosensory module with the coiled-coil linker (PSMcc) was crystallized. The structure of full-length *Is*PadC was determined from selenium single-wavelength anomalous dispersion data to 3.0 Å resolution (table S1). Two molecules of *Is*PadC are present in the asymmetric unit, revealing a parallel dimer architecture throughout the protein with a central twofold symmetry axis that is perturbed by a subtle kink of the GGDEF dimer (Fig. 1D). Almost identical parallel phytochrome dimers are observed in both dimeric species present in the higher-resolution PSMcc

structure (fig. S3). Notably, the N-terminal extension, providing the covalent attachment site for the biliverdin cofactor and extending from the characteristic figure-of-eight knot (18), interacts with parts of the hairpin/tongue region that folds back from the PHY domain to the cofactor attachment site in the GAF domain, similar to observations in Cph1 (19). The β-hairpin character of the tongue region and the conformation of the biliverdin cofactor including functionally important surrounding residues (20) (fig. S3B) show that *Is*PadC has been crystallized in its dark-adapted P_r state (fig. S4). The overall PSM monomer closely resembles that of previously published phytochrome structures [reviewed by Anders and Essen (7)], but the PSM dimer features a tighter association of the PHY domains because of their direct extension of the terminal PHY-α_5 helices with the coiled-coil linker element. Largely polar and charged residues line the dimer interface along the central helical spine, connecting the GAF and PHY domains, as well as α_5 of PHY. Starting from residue Leu[501], a characteristic coiled-coil signature is observed (fig. S1), which contains 3.5 heptad repeats that are directly extended by conserved residues of the characteristic turn preceding α_0 of GGDEF domains. The dimeric arrangement of the DGCs positions the substrate binding half active sites at the interface of the GGDEF domains, which closely resembles the overall architecture of a
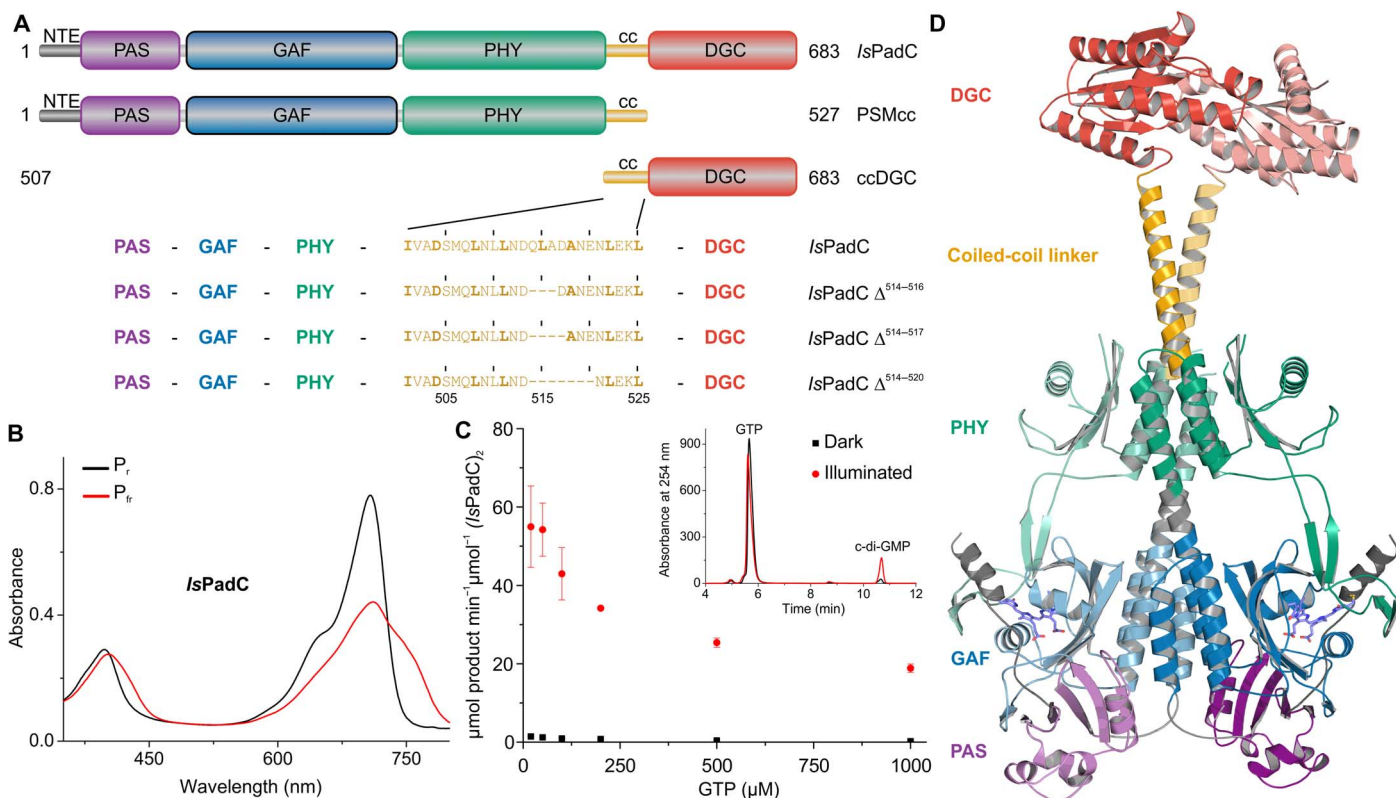

Fig. 1. Overview of *Is*PadC. (**A**) Schematic representation of *Is*PadC constructs characterized in this study. Individual domains are colored in dark gray, violet, blue, green, orange, and red for the N-terminal extension (NTE), Per-ARNT-Sim (PAS), cGMP phosphodiesterase–adenylyl cyclase–FhlA (GAF), phytochrome-associated (PHY), coiled-coil (cc), and DGC domains, respectively. Coiled-coil truncations are denoted as, for example, *Is*PadC $\Delta^{514-520}$ for the variant deleted in one heptad including residues 514 to 520. (**B**) Spectral characteristics of dark-adapted (P_r state) *Is*PadC in comparison to the P_{fr} state obtained after red light illumination. (**C**) Kinetic characterization of GTP to c-di-GMP conversion. The characteristic GTP concentration dependence of initial rates of c-di-GMP formation is indicative of substrate inhibition, which is observed for both light- and dark-state activities. Product formation was quantified in triplicate for several reaction times, and the SD of individual points contributed to the error estimation of the linear fit that is used to calculate the initial rate of product formation. The SE of the estimate from the linear regression is shown as an error bar for each GTP concentration. The inset shows representative traces of the high-performance liquid chromatography (HPLC) assay used for quantifying product formation. (**D**) Overall structure of *Is*PadC with individual domains in cartoon representation colored according to (A), with one protomer highlighted in pale colors. The biliverdin cofactor, in slate color, and its attachment site Cys[17] from the NTE are shown as stick models.

Table 1. Comparison of PadC kinetics of substrate conversion and dark-state recoveries.

Construct	Dark-state recovery at 700 nm*				Comparison of initial rates[†] at 200 μM GTP (μmol product min⁻¹ μmol⁻¹ enzyme₂)		
	τ_1 (s)	Relative A_1 (%)	τ_2 (s)	Relative A_2 (%)	Dark state	Light state	Fold activation
*Is*PadC	30 ± 1	46 ± 2	118 ± 5	54 ± 1	0.8 ± 0.1	34.2 ± 0.4	43×
*Ma*PadC	24.9 ± 0.4	50.0 ± 0.5	458 ± 56	50 ± 3	2 ± 0.2	15.4 ± 0.7	8×
*Ts*PadC	18.9 ± 0.2	80 ± 1	71 ± 3	20 ± 1	53 ± 6	42 ± 6	−1.2×
*Is*PadC $\Delta^{514-516}$	13.5 ± 0.2	40.0 ± 0.3	308 ± 12	60 ± 1	11 ± 1	10 ± 2	—
*Is*PadC $\Delta^{514-517}$	13.1 ± 0.7	11.5 ± 0.3	115 ± 1	89 ± 2	25 ± 7	49 ± 3	2×
*Is*PadC $\Delta^{514-520}$	11.9 ± 0.3	86 ± 1	393 ± 9	14.3 ± 0.1	27.2 ± 0.6	36 ± 4	1.3×
*Is*PadC $\Delta^{442-477}$::SG	n.d.[‡]	n.d.	—	—	48 ± 6	30 ± 1	−1.6×
*Is*PadC PSMcc	19 ± 1	23 ± 1	148 ± 2	77.0 ± 0.3	—	—	—
*Is*PadC ccDGC	—	—	—	—	0.2 ± 0.1		−4× (to *Is*PadC)

*Dark-state recoveries of the constructs were fit to a second-order exponential decay. After red light illumination of 1 min, changes in absorption at 700 nm were followed over 5 min, with automatic sampling every 5 s and an integration time of 0.01 s. The contribution of each phase in the dark recovery process is represented as relative amplitude. The SE of the estimate from the nonlinear curve fit corresponding to $y = A_1 * \exp(-x/\tau_1) + A_2 * \exp(-x/\tau_2) + y_0$ was used as error indicator.   †Comparison of product formation between the various constructs was performed for initial reaction rates at 50 μM GTP. Initial rates are quantified from experimental triplicates for three time points, and the SD of individual points contributed to the error estimation of the linear fit that is used to calculate the initial rate of product formation. The SE of the estimate from the linear regression is used as error indicator.   ‡The recovery of this construct could not be determined because it appears to be locked in the P_{fr}-enriched state after red light illumination and does not significantly change its spectrum during a 24-hour incubation at room temperature in the dark.

GTPαS-bound DGC dimer reported previously (21). Individual GGDEF domains superpose very well, and also the dimeric arrangement that is essential for positioning GTP for the condensation reaction is similar (fig. S5A). In line with this observation, the GTP-soaked *Is*PadC structure shows only moderate changes that are essentially restricted to a more pronounced bending of the coiled-coil linker coupled to a subtle dimer rearrangement of the GGDEF domains. A more detailed description and comparison of structural features of the three crystal structures is presented in the Supplementary Materials. Considering the additional interdomain contacts formed upon GTP binding in the dark-state *Is*PadC dimer (fig. S5B), this provides a structural rationale for the characteristic substrate inhibition observed for phytochrome-linked DGCs (Fig. 1C and fig. S2, C and D). Substrate inhibition might serve as an additional regulation mechanism for c-di-GMP synthesis, the central bacterial second messenger involved in lifestyle transitions (6), because GTP levels strongly correlate with growth conditions. However, the in vivo relevance of this observation remains to be shown.

Conformational dynamics of red light signal transduction

Because the mode of DGC regulation observed in *Is*PadC extends current concepts of activation by dimerization or product inhibition by domain immobilization (6, 15) and rather resembles recent observation for a constitutively dimeric, Zn-regulated GGDEF domain (21), we set out to characterize the in-solution conformational dynamics of dark-state and light-activated conformations using hydrogen-deuterium exchange coupled to mass spectrometry (HDX-MS). This method provides information on the conformational dynamics in various functionally relevant states (22) and hence has proven powerful in addressing signaling mechanisms in light-activated proteins (23). We performed HDX-MS of *Is*PadC under dark and constant red light conditions and, to address the functional role of the coiled-coil linker, compared

the results to experiments with the PSMcc construct (figs. S6 and S7). Figure 2 illustrates the overall effect of illumination on *Is*PadC and highlights the importance of the central helical spine of the phytochrome dimer that interacts with the coiled-coil sensor-effector linker. Only slowly exchanging amides are affected by illumination in these regions, indicating that light induces no change in α-helical structure but rather increases the conformational dynamics. Closer inspection of the region surrounding the biliverdin cofactor identifies changes in conformational dynamics of structural elements that include critical residues shown to be affected by the 15Z to 15E isomerization of the biliverdin cofactor (Fig. 2B) (16, 20). Structural rearrangements of residues surrounding the conserved DIP motif (including Asp[199]) eventually enable the structural reorganization of the tongue region (24). On the basis of the HDX data, the tongue region of *Is*PadC constitutes a moderately dynamic system that, upon illumination, increases its conformational entropy, as indicated by its rapid amide hydrogen exchange kinetics. This contrasts with observations of stable helical structures in bathy phytochromes (16) and the long-lived P_{fr} state of *Deinococcus radiodurans* phytochrome (20, 24). However, considering that the linker region shows an increase in conformational dynamics upon illumination, the loss of a stable P_r-state tongue conformation enables the structural plasticity of the PHY domains and the central helical spine to perturb the coiled-coil region (Fig. 2C and movies S1 and S2). A closer inspection of the coiled-coil composition indicates that two different helical registers can be populated by the linker element (Fig. 3). Register 1, as observed in the dark-state crystal structure, differs from register 2 only by a subtle rearrangement within the heptad units (Fig. 3, C and D). Such a rotation places the strictly conserved Asn residues (Asn[512] and Asn[519]; fig. S1) in the central *a* position of the heptad repeats and could thereby explain their functional relevance. A similar hydrogen bond–stabilized coiled-coil architecture is also observed in the prototypic GCN4 leucine zipper, and strikingly, an artificial superactive
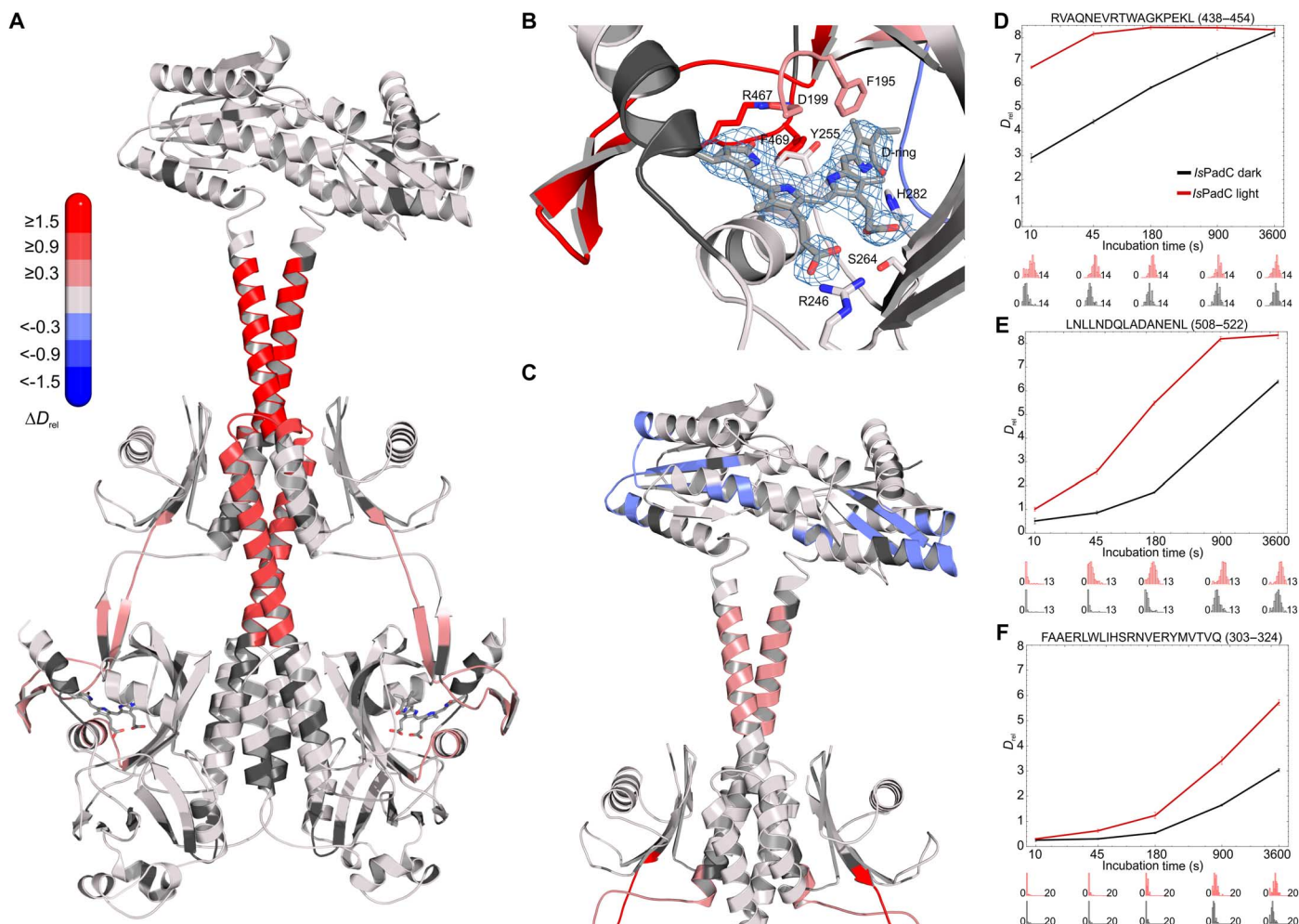
Fig. 2. Light-induced changes in conformational dynamics of full-length IsPadC observed by HDX-MS. (**A**) IsPadC structure colored according to changes in relative deuterium incorporation (ΔD_{rel}) between light-state and dark-adapted IsPadC after 15 min of deuteration (D_{rel} of IsPadC$_{light}$ − D_{rel} of IsPadC$_{dark}$). The scale bar in the top left corner indicates the changes in ΔD_{rel}, with blue corresponding to reduced deuterium incorporation and red reflecting increased exchange of amide protons upon red light illumination. The biliverdin cofactor is shown as gray stick model. (**B**) Close-up view of the biliverdin-binding pocket and the PHY tongue region. The $2F_o − F_c$ electron density map contoured at 1σ around the cofactor is shown as a light blue mesh. Important residues are shown as stick models, and the coloration corresponds to ΔD_{rel} of the 45-s exchange time point. Residues 200 to 207 were removed for clarity. However, the coloration of residues Phe[195] and Asp[199] reflect the changes in D_{rel} of the entire region 191 to 207. This region shows a higher deuterium incorporation of peptides at the interface of the PHY tongue and the biliverdin D-ring in the light state, highlighting the importance of the conformational dynamics of this region upon isomerization of the biliverdin cofactor. (**C**) Close-up view of the coiled-coil linker and the DGC domain colored according to ΔD_{rel} after 10 s of deuteration. Several structural elements of the GGDEF domain, including substrate binding elements, show a reduction in conformational dynamics upon illumination. (**D** to **F**) Deuterium uptake curves of selected IsPadC peptides, with D_{rel} plotted against the deuteration time for light- and dark-state HDX-MS experiments. The lower parts show software-estimated abundance distributions of individual deuterated species on a scale from undeuterated to all exchangeable amides deuterated. Deuteration plots for a peptide corresponding to the PHY tongue element (D), the PSM-DGC linker (E), and the internal helical spine linking the GAF and PHY domains (F). D_{rel} values are shown as the mean of three independent measurements, and error bars correspond to the SD. An overview of all analyzed peptides is provided in figs. S6 and S7.

GCN4-GGDEF fusion (*14*) features the highly conserved DXLT motif of GGDEF domains, positioned directly after the coiled-coil, in exactly the same relative orientation to the heptad architecture proposed for register 2 of IsPadC (Fig. 3, D and F). To test the involvement of coiled-coil rearrangements in regulating DGC activity, we generated variants of IsPadC that are stabilized in either register 1 or register 2 by substituting the corresponding destabilizing residues (boxed residues in Fig. 3, C and D) by either leucine or valine residues, respectively. In vivo screening of c-di-GMP production revealed that the IsPadC D504L A518L variant (stabilized in register 1) can no longer be activated by red light illumination (Fig. 3E). This contrasts with observations of the variant stabilized in register 2 (IsPadC S505V A526V) that is active un-

der both dark and red light conditions. Apparently, regulation of DGC activity is enabled by a fine-tuned balancing of the relative population of the two registers, which directly influences the positioning of functionally important residues of the GGDEF domain. In wild-type IsPadC and under dark conditions, the transition between the two registers is inhibited by the stable tongue conformation that restricts the dynamics of the central helical spine; but upon illumination, this inhibitory mechanism is released and DGC activity is increased by a more frequent population of the rotated "active" register. This conclusion is supported by an IsPadC variant deleted in the tongue region that features a substantially increased dark-state activity (Table 1 and fig. S8). Interestingly, illumination of this construct still modulates the enzymatic activity and results in
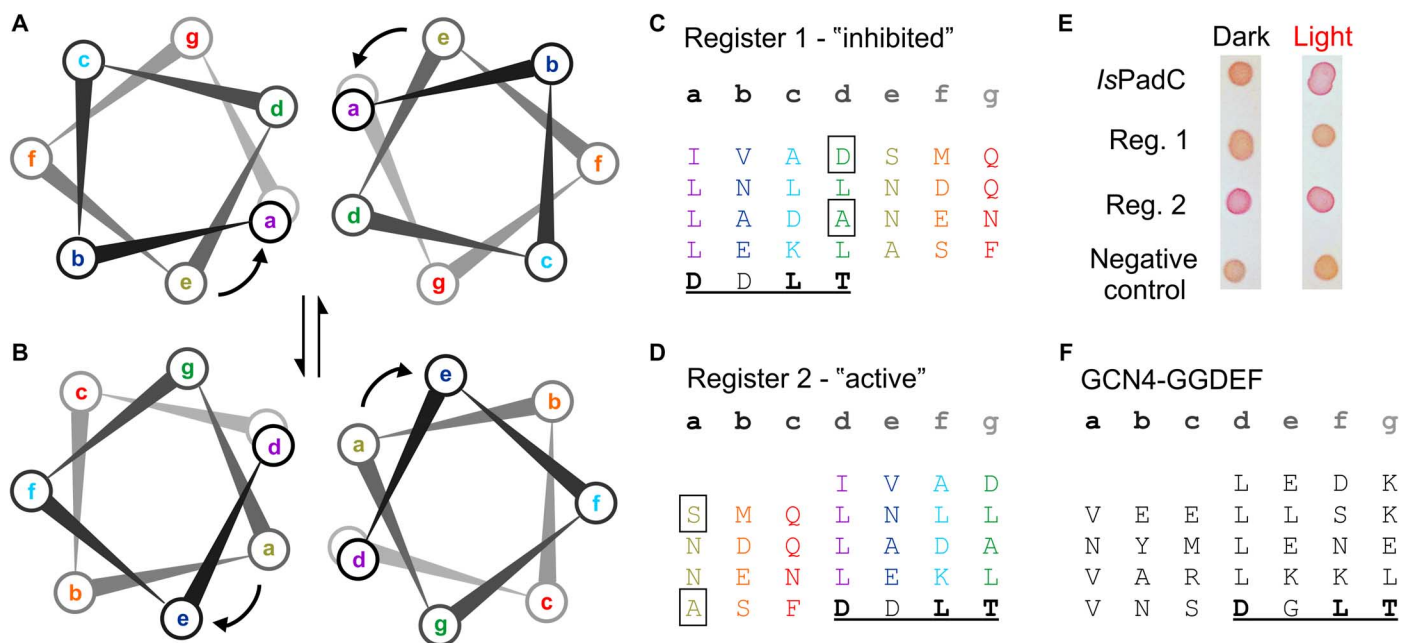
Fig. 3. Coiled-coil architecture of the sensor-effector linker. (**A**) Heptad register observed in the crystal structure of *Is*PadC (register 1). (**B**) A rotation of heptad positions *e* to *a* within the coiled-coil populates the "register 2" architecture. (**C** and **D**) Heptad units of the sensor-effector linker in registers 1 and 2, respectively, rainbow-colored according to the heptad repeats of register 1. Coiled-coil destabilizing residues are boxed. The highly conserved DXLT motif of GGDEF domains is underlined. (**E**) The assignment of active and inhibited states to registers 2 and 1, respectively, is confirmed by the observed DGC activity in a cell-based screening system. Wild-type *Is*PadC shows the expected increase in DGC activity upon red light illumination, as seen by the red coloration of the cells. In contrast, an *Is*PadC variant stabilizing register 1 can no longer be activated upon illumination, whereas the register 2 stabilizing variant is constitutively active. (**F**) For comparison, the heptad units of a superactive, artificial GCN4-GGDEF fusion (*14*) are also shown.

a reduction of DGC activity, indicating that a complex interplay of the conformational dynamics of the tongue region and the central helical spine is required for the regulation of effector domains. In this respect, it should be noted that the lack of hydrophobic packing for significant parts of the PAS-GAF dimer interface and the central helical spine is responsible for the various dimeric arrangements of PSM structures reported (*7*). The characteristic structural rearrangements of the dimer interface from a pivot point localized to the central helical spine indicate that the plasticity of this region (Fig. 4) plays an important functional role in providing the conformational flexibility to adapt to different output modules with potentially different regulatory mechanisms (*4*, *5*, *20*).

Importance of the sensor-effector linker length and composition

The conformational dynamics of the central helical spine and the coiled-coil linker are finely tuned to achieve their function in the full-length protein. In the PSMcc construct, HDX-MS analyses revealed significantly increased dynamics of the central helical regions, and hence, the composition of both the helical spine and the linker appears to have evolved to stabilize the weak dimer interfaces (PAS-GAF, PHY, and GGDEF) at their ends in the dark state (movies S3 and S4). On the basis of the characterization of truncation variants within the heptad repeats (Table 1 and fig. S8), it is apparent that not only the linker length but also the composition plays an important role. The *Is*PadC $\Delta^{514–517}$ and $\Delta^{514–520}$ deletions should allow almost identical arrangements of the effector; however, their reduced coiled-coil character and the impact of the deletions on the relative stabilities of the two coiled-coil registers observed for wild-type *Is*PadC (Fig. 3) prevent the dark-state inhibition observed for the wild-type construct. Therefore, both truncations have a reduced dynamic range of light-

regulated c-di-GMP formation. The additionally characterized *Is*PadC $\Delta^{514–516}$ construct that apparently results in a change of the relative positioning of sensor and effector preferentially produces the linear pppGpG intermediate observed in c-di-GMP biosynthesis (*25*). The ccDGC construct alone (compare Fig. 1) also catalyzes intermediate formation with lower efficiency (Table 1), suggesting that the native coiled-coil linker sequence alone is not sufficient to properly stabilize the GGDEF domains in the productive coiled-coil register. The benefit of functional regulation and prevention of futile GTP degradation has apparently led to the evolutionary generation of sensor-GGDEF couples with strong conservation of defined linker length. The central position of GTP in primary metabolism and the essential regulation of the open half active sites of GGDEF domains might be reasons for this systematic conservation in sensory GGDEF systems (*12*, *13*). PadC from *Thioalkalivibrio* sp. ALMg3 (*Ts*PadC) features an inversion of the signal, resulting in subtle light-inhibited DGC activity with an identical linker length to the *Is*PadC $\Delta^{514–520}$ variant but with different composition. Similarly, *Ma*PadC, having a seven-residue-longer linker with a charged heptad insertion, shows changes in the kinetic profile of DGC activity with less pronounced substrate inhibition. Apparently, the linker elements have been fine-tuned for their requirements not only in length but also in their amino acid composition, which likely coevolved together with other functionally relevant structural elements.

Signal transduction requires the conformational coupling of multiple structural elements

In the context of phytochrome signaling, our HDX-MS data substantiate the involvement of previously proposed functionally relevant structural elements observed in phytochromes (*10*, *16*, *17*) and support the hypothesis that observed differences in the PSM dimer architectures,
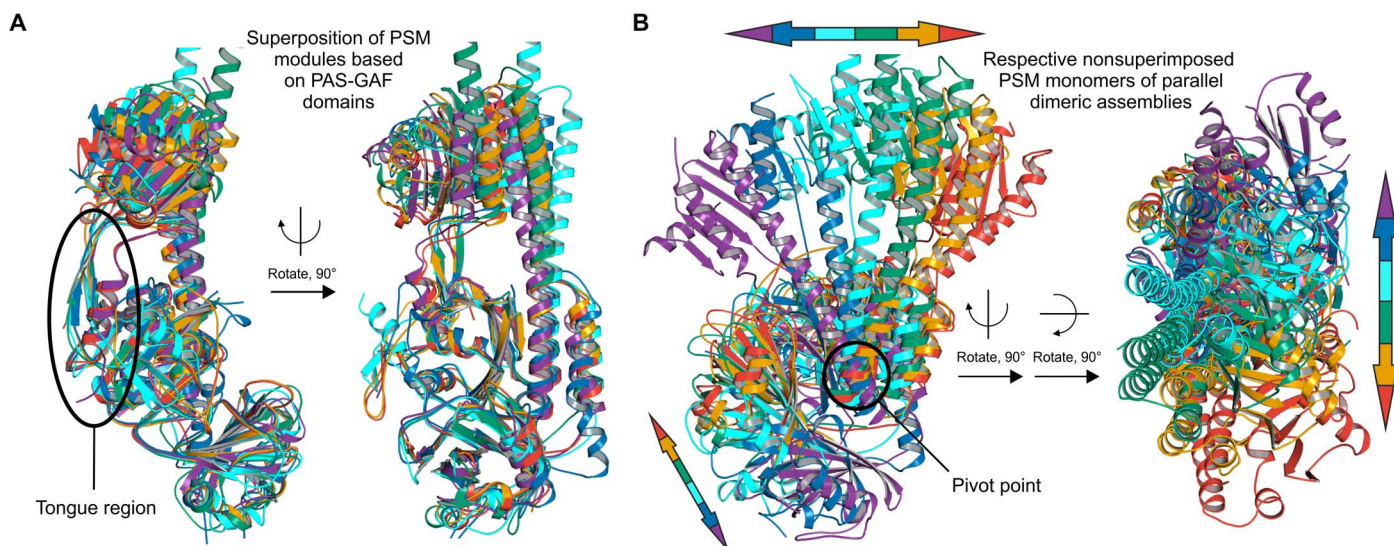
Fig. 4. Structural plasticity of phytochrome dimerization. (**A**) Superposition of PSM modules from different published phytochrome structures featuring a parallel dimeric assembly to *Is*PadC (cyan) revealed almost identical arrangements of the PAS-GAF bidomain [root mean square deviation (RMSD) of 1.5, 1.2, 1.0, 0.9, and 0.9 Å for Protein Data Bank (PDB) 4OUR_B (blue) (60), 3G6O_A (violet) (16), 4Q0J_A (orange) (61), 5AKP_B (green) (26), and 5C5K_B (red) (20), respectively]. Irrespective of the β-hairpin or α-helical character of the tongue region, the PHY domains cluster in similar positions relative to the PAS-GAF domains. However, a characteristic flexibility of the central helix connecting the GAF and PHY domains is apparent, which ultimately results in altered positioning of the terminal PHY domain helices that link to the respective output modules. (**B**) The structural plasticity of the central helical spine and, consequently, the overall parallel dimeric phytochrome assembly are even more pronounced when comparing the nonsuperposed monomers. In this case, monomers of PSM modules have been aligned to the PAS-GAF-PHY monomer of *Is*PadC chain A, and the respective other monomers are displayed (RMSD of 3.2, 2.3, 2.2, 2.2, and 1.2 Å for PDB 3G6O_A, 4Q0J_A, 5AKP_B, 5C5K_B, and 4OUR_B, respectively). Again, no clustering of the PHY domain orientation with respect to the P_r- or P_{fr}-state character of the tongue can be observed. However, the structural differences among various phytochrome dimers are nonrandom and occur along a specific trajectory that corresponds to rotation at the dimer interface. The two extremes of this rotation correspond to structures obtained for P_{fr}-state crystals (violet and red). In contrast, the only parallel phytochrome structures with adjacent C-terminal domains (green and cyan) cluster in the middle of the overall trajectory. Although this suggests that the more pronounced dimer rotation of other PSM assemblies might be due to missing interactions of their output modules and linker regions, the characteristic structural transition reflecting the plasticity of the PHY domain dimerization is very likely functionally relevant for phytochromes in general.

and the plasticity of the central PHY domain dimerization (Fig. 4), are functionally relevant. Whether the overall assembly is stabilized by an α-helical or a β-hairpin conformation of the tongue is irrelevant for the proposed model of functional phytochrome regulation (Fig. 5A) and rather reflects the evolutionary adaptation to respond to different light qualities or to modulate the dynamic range of various output modules. This is supported by the observation of increased dynamics in the P_r state of bathy phytochromes upon far-red light illumination (26), which resembles observations upon red light irradiation for all three PadC constructs characterized in this study (fig. S9), irrespective of whether they are light-activated or light-inhibited. In addition, solution-scattering studies with full-length *Is*PadC show an increased conformational flexibility between the PHY and GGDEF domains relative to the crystal structure (Fig. 5B and fig. S10). Light activation induces no pronounced, immediate structural rearrangements but a slow and reversible oligomerization process with a rate constant of 0.2 min^{-1} derived from the time-dependent increase of the small-angle x-ray scattering (SAXS)–derived molecular mass (fig. S10C). Only moderate light-induced structural changes have also recently been assigned to full-length *D. radiodurans* phytochrome (27). Therefore, the appreciation of a fine-tuned allosteric regulation mechanism following the violin model (Fig. 5) (28) will be important to appreciate general aspects of phytochrome signaling.

DISCUSSION

The consideration of a complex interplay of multiple functionally relevant structural regions helps in generalizing and understanding previously

made mechanistic proposals for long-range signal transduction in phytochromes. The importance of the tongue element and the central helical spine has been identified early on during the characterization of truncated phytochrome variants (10, 16, 17, 29, 30). However, in the absence of the corresponding output modules, the structural changes induced by illumination might not always be representative of the full-length proteins, as observed recently for *D. radiodurans* phytochrome (24, 27). For dimeric output modules, such as histidine kinases or DGCs, the functional coupling with the coiled-coil sensor-effector linker and the extended dimerization interface has important regulatory consequences for long-range signal transduction. In this respect, the similarities in overall architecture, for example, to sensors of blue light linked to histidine kinases (31) or adenylyl cyclases (32) raise the question of common principles in sensor-effector coupling. Although this is one of the central questions in understanding the astonishing modularity of naturally evolved sensor-effector systems, the divergence of postulated mechanisms even within individual sensory modules currently prevents a unifying answer. However, appreciation of a regulatory mechanism in line with the violin model (28) allows the conclusion that multiple output mechanisms can be realized within the same overall architecture. For example, removal of the tongue region in *Is*PadC still allows regulation of the effector module via the central helical spine, a signaling route used by evolutionary-related cyanobacteriochrome systems (33). Along this line, even anti-parallel dimers or phytochrome monomers might be functionally relevant in different systems; for example, the binding of monomeric *Rhodopseudomonas palustris* phytochrome 1 to PpsR dimers, in analogy to blue light photoreceptors, shows interesting parallels to molecular principles identified for the AppA-PpsR system (34, 35). Consequently,
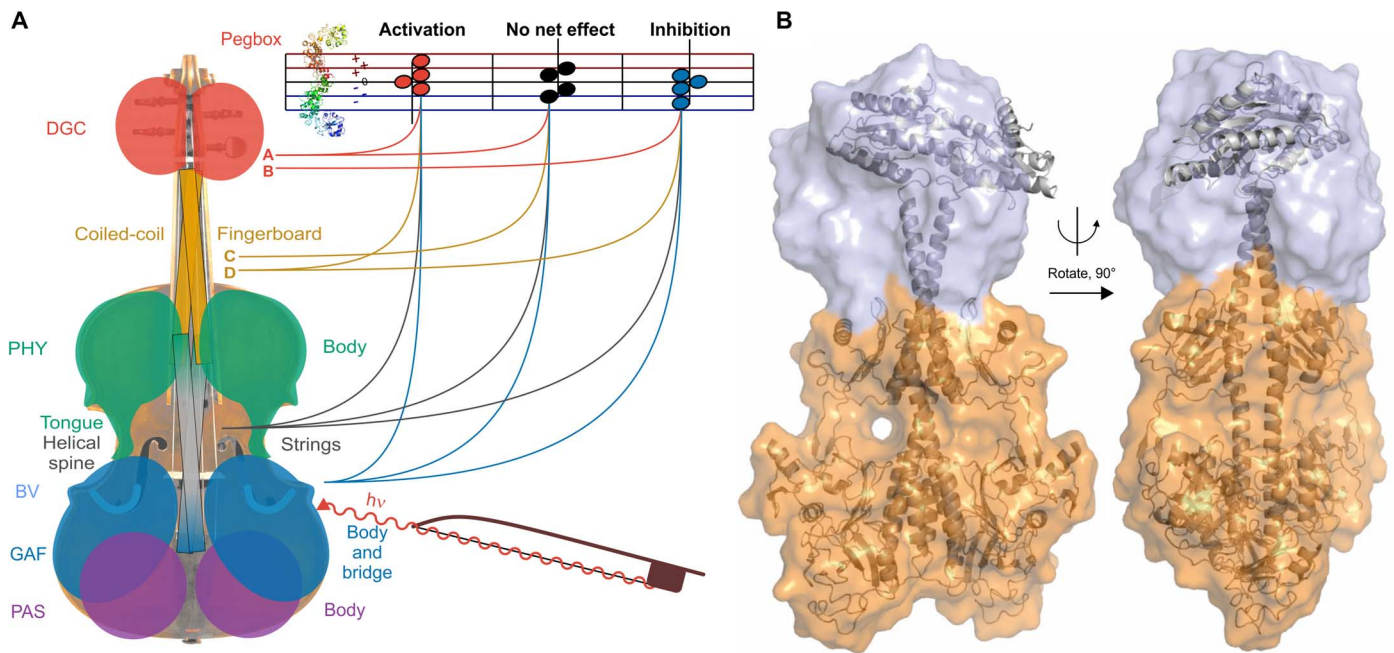
Fig. 5. Schematic model of signal integration pathways in phytochrome-linked enzymatic effectors and in-solution structure of *Is*PadC. (**A**) The characteristic structure of *Is*PadC and regulatory properties of closely related homologs suggest a model of signal transduction corresponding to the violin model (*28*). Instead of a linear cascade of structural changes resulting in enzyme activation, the conformational dynamics of the whole system define the population of functionally relevant states, leading to either activation or inactivation with similar overall architectures (*37*). In the case of the phytochrome-violin, the pegbox corresponds to the effector domain, whose activity is tuned by the sensory module. Hitting the right chords on the enzymatic activity clef for stimulating GTP turnover is more complex than a specific actuation of the fingerboard, which would correspond to, for example, variation of its length (yellow lines and linkers C and D), and additionally depends on properties of the strings (gray), the shape of the violin body (blue), and the effector-pegbox (red; for example, two different DGC constructs A and B). The characteristic structural changes observed for various phytochrome structures (Fig. 4), which had also been interpreted as specific light-induced rearrangements (*20*, *24*), reflect the structural plasticity of phytochrome dimerization. The latter, in turn, enables the modulation of the conformational dynamics of the overall system and thereby allows complex, evolutionary fine-tuning of the body of phytochrome-violin to optimize the output functionality as required by each system. The absence of characteristic structural changes, such as a defined rotation or a separation of the coiled-coil linker, enables the realization of systems featuring activation or inactivation within the same molecular architecture. (**B**) SAXS-based structural model for the *Is*PadC dimer in its dark-adapted P$_r$ state. The surface represents the conformational space sampled by the GGDEF domains in the seven best structures according to the fit between the experimental and back-calculated SAXS data (compare fig. S10). Structures are aligned to the PAS-GAF-PHY domains.

even molecular details of long-range signal transduction in parallel dimeric phytochrome systems might not be conserved in every detail. Although a precise register switching and a characteristic length of the coiled-coil appear important for the regulation of GGDEF domains, the requirements for functional regulation of other enzymatic functionalities might feature different molecular characteristics such as regulated unfolding (*36*) or large-scale rotational mechanisms (*20*, *27*).

As far as phytochrome engineering for direct allosteric regulation of effector domains is concerned, our results show that the natural selection of linker length does not necessarily correlate with a high dynamic range that would be desirable for optogenetic tools. Therefore, an improved understanding of the effect of linker length and composition variations on phytochrome signaling and how this eventually translates into molecular mechanisms of regulation for various effector domains will be required to enable a more rational design approach. Especially the observation of signal inversion for closely related systems suggests that an ensemble of differently populated functionally relevant states with differing energies needs to be considered (*37*). In this respect, the observation of two helical registers for phytochrome-linked DGCs and the modulation of their relative population upon activation provide an interesting perspective for interpreting successful and unsuccessful rationally designed sensor-effector fusions. Similar regulatory effects of transitions between different coiled-coil registers have been observed for mediating cargo binding to dynein by BicD (*38*) as well as modulating

interactions of the cell cycle regulator Nek2 (*39*). In the context of long-range signaling, another interesting parallel is the rotary mechanism proposed for transmembrane signaling and its integration by HAMP domains (*40*). However, considering the dynamic properties of these coiled-coil structures, it will be interesting to see whether the major contribution to regulation is the rotary forces induced by the register switch or rather the conformational dynamics during the continuous transition between energetically similar coiled-coil registers. The latter mechanism has recently been shown to be critical for functional protein-protein interactions in the case of streptococcal M proteins (*41*). In the context of phytochrome-regulated DGCs, the involvement of energetically similar coiled-coil registers could also provide a rationale for the evolutionary adaptation of the dynamic range of light activation by altering the coiled-coil composition as well as by modifying structural elements that are functionally coupled to the sensor-effector linker.

In summary, we show that phytochrome regulation depends on the molecular characteristics of the central helical spine, the tongue region, and the coiled-coil linker region. We provide initial insights into the relative contributions of various sensor-effector elements to the energetic coupling of individual domains (*42*) that will eventually allow a better understanding of molecular mechanisms involved in phytochrome signaling. The appreciation of dynamically driven allostery (*43*) and the possibility to both activate and inhibit enzymatic activity in similar systems allow the conclusion that the rational design of sensor-effector

couples needs to consider functional aspects of both sensor and effector domains that are inherently linked to their conformational dynamics.

MATERIALS AND METHODS
Protein expression and purification
The coding sequences of PadC homologs from *Idiomarina* sp. A28L, *Marinimicrobium agarilyticum*, and *Thioalkalivibrio* sp. ALMg3 (sequence accession numbers WP_007419415, WP_027329460, and WP_026331574, respectively) corresponding to *Is*PadC, *Ma*PadC, and *Ts*PadC were synthesized with codon optimization for expression in *Escherichia coli* (GeneArt, Life Technologies). Gene cassettes were cloned into the pETM-11 vector by restriction ligation using the Nco I and Not I sites for expression with a tobacco etch virus (TEV)–cleavable polyhistidine tag. Truncation variants of *Is*PadC were produced by site-directed mutagenesis following the protocol described by Liu and Naismith (44) (primers used in this work are listed in table S2A).

PadC variants were produced as $(His)_6$-tagged holoproteins in complex with the biliverdin chromophore in *E. coli* BL21 (DE3) by co-expression of heme oxygenase (HO-1) from *Synechocystis* sp. PCC6803. For this purpose, we replaced the kanamycin cassette of pT7-ho1 (9) with the chloramphenicol resistance marker of pACYC184. Cells grown to mid-log phase at 37°C in LB medium supplemented with 0.3% glucose and 8.3 mM $MgCl_2$ were shifted to 16°C for induction with 0.25 mM isopropyl-β-D-thiogalactopyranoside (IPTG) for ~15 hours in the presence of δ-aminolevulinic acid (10 mg liter^{-1}). After harvesting, cells were disrupted in lysis buffer (compare table S2B) by combining lysozyme (100 µg ml^{-1}) and sonication (2 × 5 min, 100 W, continuous mode; Labsonic L, Sartorius). Lysates were clarified by ultracentrifugation (206,000g) and affinity-purified on a Ni^{2+}-Sepharose matrix (Ni Sepharose 6 Fast Flow, GE Healthcare) by gravity flow in a Protino column (Macherey-Nagel). After sample loading, proteins were washed with lysis buffer supplemented with 40 mM imidazole and finally eluted with 250 mM imidazole containing lysis buffer. Eluted fractions were then subjected to overnight dialysis (table S2B) in the presence of TEV protease at a ratio of ~1:16 for TEV/substrate. The histidine-tagged TEV protease and the cleaved histidine tag were removed by reloading the dialyzed sample onto the Ni^{2+} column and collecting the flow through. After concentration (Amicon Ultra-15, Merck Millipore), PadC samples were purified by size-exclusion chromatography on a 16/60 Superdex 200 prep grade column (GE Healthcare) with buffers according to table S2B. The purified proteins were concentrated, aliquoted, flash-frozen in liquid nitrogen, and conserved at −80°C until needed.

Selenomethionine-substituted *Is*PadC was expressed in *E. coli* BL21 (DE3) coexpressing heme oxygenase using modified minimal growth medium containing increased concentrations of certain amino acids for metabolic inhibition of methionine biosynthesis (45) and purified following the procedure described above.

The *Is*PadC ccDGC construct was initially purified in its c-di-GMP–bound form. To obtain product-free protein preparations, samples were incubated with the phosphodiesterase RocR and repurified by a third Ni column step to remove His-tagged RocR and by gel filtration to remove the pGpG product from the phosphodiesterase reaction. Purification of RocR was performed as previously described by Rao *et al.* (46) using the affinity purification materials described above.

Cell-based DGC assay
DGC activity was screened by adaptation of a previously described protocol (47). *E. coli* BL21 (DE3) cells containing the pT7-ho1 helper plasmid and transformed with pETM-11–based PadC expression plasmids were grown at 30°C in YESCA medium [casamino acids (10 mg ml^{-1}) and yeast extract (1.5 mg ml^{-1})] supplemented with $MgSO_4$ (0.05 mg ml^{-1}), $FeSO_4$ (0.5 µg ml^{-1}), kanamycin (30 µg ml^{-1}), and chloramphenicol (34 µg ml^{-1}) to an absorbance of 0.5 at 600 nm. Each culture was then induced with 0.25 mM IPTG and δ-aminolevulinic acid (10 mg liter^{-1}) for 4 hours at 16°C. Afterward, 3 µl of the induced culture was spotted on YESCA agar plates containing kanamycin (30 µg ml^{-1}), chloramphenicol (34 µg ml^{-1}), and Congo red (0.01 mg ml^{-1}) and incubated at 20°C for 16 hours in the dark or under constant red light illumination (75 µW cm^{-2} at 630 nm). As a negative control, we used a pETM-11 AppA construct (35) that does not show any DGC activity.

Spectroscopic characterization
Ultraviolet (UV)–visible absorption spectra were acquired with a Specord 200 Plus spectrophotometer (Analytik Jena) using protein samples diluted in their corresponding storage buffers (compare table S2B). Dark-adapted P_r-state absorption spectra were measured from samples equilibrated under nonactinic conditions and minimizing the contact time with measuring light. P_{fr}-enriched spectra were recorded immediately after red light irradiation [1.8 mW cm^{-2} at 630 nm; Luminea light-emitting diode (LED)] using a charge-coupled device (CCD)–based Flame spectrometer (Ocean Optics) with low-intensity measuring light (mercury-xenon lamp). All spectra and time course experiments were measured at room temperature.

P_r-state recovery kinetics were followed at 700 and 750 nm after 1 min of red light illumination. Integration times and time intervals of the time scans were adjusted for the individual variants to minimize the effect of the actinic measuring lights. Reported time constants of dark-state recovery differ by less than 10% between 700- and 750-nm recordings.

Crystallization and structure elucidation
Dark-adapted *Is*PadC was crystallized at 289 K using a hanging-drop vapor diffusion setup. Drops (2 µl) containing equal volumes of protein solution at 7 mg/ml and reservoir solution [0.1 M bis-tris (pH 5.5), 0.1 M ammonium acetate, 17% (w/v) polyethylene glycol 10,000] were equilibrated against 500 µl of reservoir solution. Plate-like elongated crystals appeared after overnight incubation under dark conditions and reached final dimensions within 5 days. Pronounced drop-to-drop variability in crystallization behavior was observed, and some initially clear drops produced differently shaped crystals during prolonged incubation (~1 month). Structure elucidation revealed that these crystals correspond to a proteolytic degradation product corresponding to the *Is*PadC PSMcc fragment. Crystals were harvested from 2-µl drops equilibrated against 35 µl of reservoir solution in a sitting-drop vapor diffusion setup as described for full-length *Is*PadC.

Crystals of selenomethionine-labeled *Is*PadC were obtained following the same protocol as for native *Is*PadC in the presence of 1 mM dithioerythritol and were collected after 15 days of crystal growth. Crystals were harvested under low-intensity green light conditions (520 ± 20 nm LED) by transferring to a cryoprotectant solution (reservoir solution containing 25% glycerol) and subsequent flash-freezing in liquid nitrogen. GTP soaks of full-length *Is*PadC crystals were performed by a 5-min incubation in the cryoprotectant solution supplemented with 10 mM GTP (Roth) under nonactinic light conditions. Diffraction data for native and Se-Met *Is*PadC were collected at beamlines ID29-10 and ID23-1, respectively, of the European Synchrotron Radiation Facility (ESRF). Data were processed using the XDS program

package (48), and Se-Met data sets collected at multiple positions were merged for successful phasing by selenium single-wavelength anomalous dispersion (table S1).

The crystal structure of IsPadC was solved by a combination of molecular replacement and single-wavelength anomalous dispersion phasing. Because of the moderate quality of the initial anomalous electron density map obtained from the 3 Å Se-Met data set with PHENIX AutoSol (49), individual search models of the PAS-GAF, PHY, and GGDEF domains were generated using PHENIX Sculptor (50) on the basis of the IsPadC sequence and the structures of the PAS-GAF module from R. palustris bacteriophytochrome RpA3015 (PDB 4S21) (30), the structure of the PHY domain of bacteriophytochrome RpBphP3 from R. palustris (PDB 4R70) (30), and the structure of the GGDEF domain of WpsR from Pseudomonas aeruginosa (PDB 3I5B) (14), respectively. Two molecules of each search model were successfully placed in the asymmetric unit using PHENIX Phaser (51). The initial model of a PAS-GAF-PHY-GGDEF dimer was subsequently used for rigid-body fitting in the anomalous density map and refined in several rounds of maximum likelihood least-squares refinement of models modified with Coot using σ_A-weighted $2mF_o - DF_c$ and $F_o - F_c$ electron density maps. Refinement included experimental phase information using a phased maximum likelihood target (MLHL). In addition, torsion noncrystallographic symmetry (NCS) restraints and secondary structure restraints were included together with Translation/Libration/Screw (TLS) groups for the individual domains of the protein. During the final rounds of refinement, reference model restraints from the higher-resolution PSMcc structure were included.

The crystal structure of IsPadC PSMcc fragment was solved by molecular replacement using PHENIX Phaser with an intermediate model of the PAS-GAF-PHY fragment from the full-length structure of IsPadC as search model. Refinement included an initial simulated annealing (torsion) step followed by several rounds of maximum likelihood least-squares refinement of models modified with Coot, as described above. TLS and secondary structure restraints were applied during the refinement.

The crystal structure of IsPadC soaked with GTP was solved by molecular replacement using PHENIX Phaser with models of the dimeric IsPadC PSM containing the coiled-coil linker and the dimer of the IsPadC DGC. Refinement included an initial rigid-body fit of individual domains because the linker element revealed a more pronounced kink in the soak crystal, followed by several rounds of maximum likelihood least-squares refinement of models modified with Coot, as described above. TLS, NCS, and secondary restraints were applied during the refinement.

Kinetic characterization of PadC constructs
To monitor the conversion of GTP to c-di-GMP, we used an HPLC-based assay adapted from Enomoto et al. (11). Briefly, appropriate amounts of enzyme were incubated with various GTP concentrations at 20°C in reaction buffer containing 50 mM Hepes (pH 7.0), 150 mM NaCl, and 50 mM MgCl$_2$. Reactions were stopped at different time points by heat denaturation at 95°C for 1 min. Samples were cleared by centrifugation, and the supernatant was subjected to HPLC analysis using a reversed-phase column (SunFire C18 4.6 mm × 100 mm, Waters) equilibrated in 10 mM triethylammonium formate (pH 6.0). Substrate and product were separated using a linear, 23-min gradient from 2 to 20% MeOH at a flow rate of 1 ml min^{-1}. To remove inhibitory components from the GTP stock (Roth), it was initially purified by HPLC using a similar protocol. GTP (25 mg) was dissolved in 10 mM Hepes (pH 7.0) and purified in several runs over a preparative HPLC column (SunFire C18 10 mm × 100 mm, Waters) equilibrated in 10 mM triethylammonium formate (pH 6.0) using a MeOH gradient from 10 to 100%. Purified GTP fractions were then lyophilized and resuspended in 10 mM Hepes (pH 7.0) with final adjustment to a pH between 7 and 8. For the following red light–activated reactions, samples were preilluminated (0.7 mW cm^{-2} at 630 nm, Luminea LED) for 1 min before starting the reaction and maintained under constant illumination during the course of the reaction. For quantification of c-di-GMP formation, all samples were corrected for the amount of product formed during the heat inactivation step. The identity of the c-di-GMP peak was confirmed by MS, and the linear intermediate was identified by collecting representative fractions and verifying subsequent conversion to c-di-GMP by wild-type IsPadC. All activities were normalized to the dimer concentrations of the respective constructs.

Hydrogen-deuterium exchange coupled to mass spectrometry
Deuterium-labeling experiments were performed to address the effect of illumination on the conformational dynamics of full-length IsPadC and functional fragments thereof. Proteins were diluted to a final concentration of 200 µM in their storage buffers (compare table S2B) under nonactinic light conditions. Aliquots (2.5 µl) were preequilibrated at 20°C for 1 min under dark conditions or with red light illumination (0.7 mW cm^{-2} at 630 nm, Luminea LED), and the deuterium-labeling reaction started by 20-fold dilution in D$_2$O containing 10 mM Hepes (pD 7.0), 150 mM NaCl, and 10 mM MgCl$_2$. Aliquots (5 µl) were removed after 10 s, 45 s, 3 min, 15 min, and 60 min and quenched with 50 µl of ice-cold 200 mM ammonium formic acid (pH 2.5). The quenched labeling reaction (50 µl) was injected into a cooled HPLC setup, as described previously (52). Briefly, deuterated samples were digested on an immobilized pepsin column (Poroszyme, Applied Biosystems) operated at 10°C. Resulting peptides were desalted on a 2-cm C18 guard column (DiscoveryBIO C18, Sigma) and separated during a 7-min acetonitrile gradient (15 to 50%) in the presence of 0.6% (v/v) formic acid on a reversed-phase column (XR ODS 75 mm × 3 mm, 2.2 µM; Shimadzu). Peptides were then infused into a maXis electrospray ionization ultrahigh-resolution time-of-flight (UHR-TOF) mass spectrometer (Bruker). Deuterium incorporation was analyzed and quantified using the Hexicon 2 software package (http://hx2.mpimf-heidelberg.mpg.de) (53).

Limited proteolysis
Trypsin digestion patterns of all three PadC homologs were obtained by following the proteolytic degradation over 60 min in the dark or with constant red light illumination (0.7 mW cm^{-2} at 630 nm, Luminea LED) at 20°C. A 1:100 (w/w) ratio of protease to enzyme was used for IsPadC, 1:750 (w/w) ratio for MaPadC, and 1:1000 (w/w) ratio for TsPadC with PadC concentrations varying between 6 and 8 µM. Tryptic digests were performed in reaction buffer containing 10 mM tris-HCl (pH 8.0), 500 mM NaCl, and 10 mM MgCl$_2$. PadC (5 µg) was quenched per time point upon mixing with SDS sample buffer [4× stock: 10% (w/v) glycerol, 0.6% (w/v) tris-HCl (pH 6.8), 2% (w/v) SDS, 0.02% (w/v) bromophenol blue, 1.5% (w/v) dithiothreitol] and heating at 95°C for 5 min. All samples were loaded onto a 12% SDS–polyacrylamide gel for electrophoretic separation of proteolytic fragments.

Small-angle x-ray scattering
SAXS data for solutions of IsPadC in the light and dark states were recorded on an in-house SAXS instrument (SAXSess mc^2, Anton Paar)

equipped with a Kratky camera, a sealed x-ray tube source, and a two-dimensional Princeton Instruments PI•SCX:4300 (Roper Scientific) CCD detector. For dark- and light-state measurements, the protein solutions were either kept in the dark or exposed to red light (1.8 mW cm^{-2} at 630 nm, Luminea LED) for 90 min before the measurements. The scattering patterns were measured with a 180-min exposure time (1080 frames, 10 s each) for several solute concentrations ranging from 0.8 to 13.0 mg/ml (fig. S10). Radiation damage was excluded on the basis of a comparison of individual frames of the 180-min exposures, where no changes were detected. A range of momentum transfer of 0.012 Å^{-1} < s < 0.63 Å^{-1} was covered [$s = 4\pi \sin(\theta)/\lambda$, where 2θ is the scattering angle and $\lambda = 1.542$ Å is the x-ray wavelength].

All SAXS data were analyzed with the package ATSAS (version 2.5). The data were processed with the SAXSQuant software (version 3.9) and desmeared using the programs GNOM and GIFT (54, 55). The forward scattering $I(0)$, the radius of gyration R_g, the maximum dimension D_{max}, and the interatomic distance distribution functions [$P(R)$] were computed with the program GNOM (54). The masses of the solutes were evaluated by comparison of the forward scattering intensity with that of a human serum albumin reference solution (molecular mass, 69 kDa) and using Porod's law. To generate ab initio shape models, a total of 50 models were calculated using the program DAMMIF (56) and aligned and averaged using the program DAMCLUST. C2 symmetry was defined. The ab initio shape models were aligned with the crystal structure of *Is*PadC using the program SUPCOMB (57). The structures of *Is*PadC were modeled using the program CORAL (58). Input was the crystal structure of *Is*PadC determined here and SAXS data. The orientation of the DGC domains was kept flexible during the calculations, and no dimerization interface was restrained to account for dynamics. A total of 50 structures were calculated, and the best structures based on the fit to the experimental data were selected to prepare the figures.

SUPPLEMENTARY MATERIALS

Supplementary material for this article is available at http://advances.sciencemag.org/cgi/content/full/3/2/e1602498/DC1

Supplementary Results

fig. S1. Multiple sequence alignment of PadC homologs generated with Jalview (64).
fig. S2. Spectroscopic and kinetic characterization of *Ts*PadC and *Ma*PadC.
fig. S3. Characterization of the *Is*PadC PSMcc variant.
fig. S4. *Is*PadC crystal and spectral characteristics of dark-state crystallized *Is*PadC.
fig. S5. Effect of substrate binding on the overall architecture of *Is*PadC.
fig. S6. Summary of HDX experiments.
fig. S7. Individual deuterium incorporation plots of all evaluated peptides.
fig. S8. Spectroscopic and kinetic characterization of *Is*PadC deletion variants.
fig. S9. Time course of tryptic digests of *Is*PadC, *Ma*PadC, and *Ts*PadC under dark and light conditions.
fig. S10. Details of SAXS measurements.
table S1. Data collection, phasing, and refinement statistics.
table S2. Overview of oligonucleotides and buffers.
movie S1. Changes in conformational dynamics upon red light illumination of *Is*PadC.
movie S2. Changes in conformational dynamics upon red light illumination of the *Is*PadC PSMcc variant.
movie S3. The influence of effector deletion on conformational dynamics of the dark-state *Is*PadC PSMcc assembly.
movie S4. The influence of effector deletion on conformational dynamics of the light-state *Is*PadC PSMcc assembly.
References (62–66)

REFERENCES AND NOTES

1. D. Tischer, O. D. Weiner, Illuminating cell signalling with optogenetic tools. *Nat. Rev. Mol. Cell Biol.* **15**, 551–558 (2014).
2. G. P. Pathak, J. D. Vrana, C. L. Tucker, Optogenetic control of cell function using engineered photoreceptors. *Biol. Cell* **105**, 59–72 (2013).
3. K. D. Piatkevich, F. V. Subach, V. V. Verkhusha, Engineering of bacterial phytochromes for near-infrared imaging, sensing, and light-control in mammals. *Chem. Soc. Rev.* **42**, 3441–3452 (2013).
4. M.-H. Ryu, I.-H. Kang, M. D. Nelson, T. M. Jensen, A. I. Lyuksyutova, J. Siltberg-Liberles, D. M. Raizen, M. Gomelsky, Engineering adenylate cyclases regulated by near-infrared window light. *Proc. Natl. Acad. Sci. U.S.A.* **111**, 10167–10172 (2014).
5. C. Gasser, S. Taiber, C. M. Yeh, C. H. Wittig, P. Hegemann, S. Ryu, F. Wunder, A. Möglich, Engineering of a red-light–activated human cAMP/cGMP-specific phosphodiesterase. *Proc. Natl. Acad. Sci. U.S.A.* **111**, 8803–8808 (2014).
6. U. Römling, M. Y. Galperin, M. Gomelsky, Cyclic di-GMP: The first 25 years of a universal bacterial second messenger. *Microbiol. Mol. Biol. Rev.* **77**, 1–52 (2013).
7. K. Anders, L.-O. Essen, The family of phytochrome-like photoreceptors: Diverse, complex and multi-colored, but very useful. *Curr. Opin. Struct. Biol.* **35**, 7–16 (2015).
8. D. A. Ryjenkov, M. Tarutina, O. V. Moskvin, M. Gomelsky, Cyclic diguanylate is a ubiquitous signaling molecule in bacteria: Insights into biochemistry of the GGDEF protein domain. *J. Bacteriol.* **187**, 1792–1798 (2005).
9. M. Tarutina, D. A. Ryjenkov, M. Gomelsky, An unorthodox bacteriophytochrome from *Rhodobacter sphaeroides* involved in turnover of the second messenger c-di-GMP. *J. Biol. Chem.* **281**, 34751–34758 (2006).
10. K. Anders, G. Daminelli-Widany, M. A. Mroginski, D. von Stetten, L.-O. Essen, Structure of the cyanobacterial phytochrome 2 photosensor implies a tryptophan switch for phytochrome signaling. *J. Biol. Chem.* **288**, 35714–35725 (2013).
11. G. Enomoto, R. Nomura, T. Shimada, N.-N. Win, R. Narikawa, M. Ikeuchi, Cyanobacteriochrome SesA is a diguanylate cyclase that induces cell aggregation in *Thermosynechococcus*. *J. Biol. Chem.* **289**, 24801–24809 (2014).
12. S. T. Glantz, E. J. Carpenter, M. Melkonian, K. H. Gardner, E. S. Boyden, G. Ka-Shu Wong, B. Y. Chow, Functional and topological diversity of LOV domain photoreceptors. *Proc. Natl. Acad. Sci. U.S.A.* **113**, E1442–E1451 (2016).
13. A. Möglich, R. A. Ayers, K. Moffat, Structure and signaling mechanism of Per-ARNT-Sim domains. *Structure* **17**, 1282–1294 (2009).
14. N. De, M. V. A. S. Navarro, R. V. Raghavan, H. Sondermann, Determinants for the activation and autoinhibition of the diguanylate cyclase response regulator WspR. *J. Mol. Biol.* **393**, 619–633 (2009).
15. T. Schirmer, U. Jenal, Structural and mechanistic determinants of c-di-GMP signalling. *Nat. Rev. Microbiol.* **7**, 724–735 (2009).
16. X. Yang, J. Kuk, K. Moffat, Conformational differences between the Pfr and Pr states in *Pseudomonas aeruginosa* bacteriophytochrome. *Proc. Natl. Acad. Sci. U.S.A.* **106**, 15639–15644 (2009).
17. E. S. Burgie, R. D. Vierstra, Phytochromes: An atomic perspective on photoactivation and signaling. *Plant Cell* **26**, 4568–4583 (2014).
18. J. R. Wagner, J. S. Brunzelle, K. T. Forest, R. D. Vierstra, A light-sensing knot revealed by the structure of the chromophore-binding domain of phytochrome. *Nature* **438**, 325–331 (2005).
19. L.-O. Essen, J. Mailliet, J. Hughes, The structure of a complete phytochrome sensory module in the Pr ground state. *Proc. Natl. Acad. Sci. U.S.A.* **105**, 14709–14714 (2008).
20. E. S. Burgie, J. Zhang, R. D. Vierstra, Crystal structure of *Deinococcus* phytochrome in the photoactivated state reveals a cascade of structural rearrangements during photoconversion. *Structure* **24**, 448–457 (2016).
21. F. Zähringer, E. Lacanna, U. Jenal, T. Schirmer, A. Boehm, Structure and signaling mechanism of a zinc-sensory diguanylate cyclase. *Structure* **21**, 1149–1157 (2013).
22. L. Konermann, J. Pan, Y.-H. Liu, Hydrogen exchange mass spectrometry for studying protein structure and dynamics. *Chem. Soc. Rev.* **40**, 1224–1234 (2011).
23. R. Lindner, U. Heintz, A. Winkler, Applications of hydrogen deuterium exchange (HDX) for the characterization of conformational dynamics in light-activated photoreceptors. *Front. Mol. Biosci.* **2**, 33 (2015).
24. H. Takala, A. Björling, O. Berntsson, H. Lehtivuori, S. Niebling, M. Hoernke, I. Kosheleva, R. Henning, A. Menzel, J. A. Ihalainen, S. Westenhoff, Signal amplification and transduction in phytochrome photosensors. *Nature* **509**, 245–248 (2014).
25. P. Ross, H. Weinhouse, Y. Aloni, D. Michaeli, P. Weinberger-Ohana, R. Mayer, S. Braun, E. de Vroom, G. A. van der Marel, J. H. van Boom, M. Benziman, Regulation of cellulose synthesis in *Acetobacter xylinum* by cyclic diguanylic acid. *Nature* **325**, 279–281 (1987).
26. L. H. Otero, S. Klinke, J. Rinaldi, F. Velázquez-Escobar, M. A. Mroginski, M. Fernández López, A. Malamud, A. A. Vojnov, P. Hildebrandt, F. A. Goldbaum, H. R. Bonomi, Structure of the full-length bacteriophytochrome from the plant pathogen *Xanthomonas campestris* provides clues to its long-range signaling mechanism. *J. Mol. Biol.* **428**, 3702–3720 (2016).
27. A. Björling, O. Berntsson, H. Lehtivuori, H. Takala, A. J. Hughes, M. Panman, M. Hoernke, S. Niebling, L. Henry, R. Henning, I. Kosheleva, V. Chukharev, N. V. Tkachenko, A. Menzel, G. Newby, D. Khakhulin, M. Wulff, J. A. Ihalainen, S. Westenhoff, Structural photoactivation of a full-length bacterial phytochrome. *Sci. Adv.* **2**, e1600920 (2016).
28. A. P. Kornev, S. S. Taylor, Dynamics-driven allostery in protein kinases. *Trends Biochem. Sci.* **40**, 628–647 (2015).

29. X. Yang, J. Kuk, K. Moffat, Crystal structure of *Pseudomonas aeruginosa* bacteriophytochrome: Photoconversion and signal transduction. *Proc. Natl. Acad. Sci. U.S.A.* **105**, 14715–14720 (2008).

30. X. Yang, E. A. Stojković, W. B. Ozarowski, J. Kuk, E. Davydova, K. Moffat, Light signaling mechanism of two tandem bacteriophytochromes. *Structure* **23**, 1179–1189 (2015).

31. R. P. Diensthuber, M. Bommer, T. Gleichmann, A. Möglich, Full-length structure of a sensor histidine kinase pinpoints coaxial coiled coils as signal transducers and modulators. *Structure* **21**, 1127–1136 (2013).

32. M. Ohki, K. Sugiyama, F. Kawai, H. Tanaka, Y. Nihei, S. Unzai, M. Takebe, S. Matsunaga, S.-i. Adachi, N. Shibayama, Z. Zhou, R. Koyama, Y. Ikegaya, T. Takahashi, J. R. H. Tame, M. Iseki, S.-Y. Park, Structural insight into photoactivation of an adenylate cyclase from a photosynthetic cyanobacterium. *Proc. Natl. Acad. Sci. U.S.A.* **113**, 6659–6664 (2016).

33. C. C. Cornilescu, G. Cornilescu, E. S. Burgie, J. L. Markley, A. T. Ulijasz, R. D. Vierstra, Dynamic structural changes underpin photoconversion of a blue/green cyanobacteriochrome between its dark and photoactivated states. *J. Biol. Chem.* **289**, 3055–3065 (2014).

34. D. Bellini, M. Z. Papiz, Structure of a bacteriophytochrome and light-stimulated protomer swapping with a gene repressor. *Structure* **20**, 1436–1446 (2012).

35. A. Winkler, U. Heintz, R. Lindner, J. Reinstein, R. L. Shoeman, I. Schlichting, A ternary AppA–PpsR–DNA complex mediates light regulation of photosynthesis-related gene expression. *Nat. Struct. Mol. Biol.* **20**, 859–867 (2013).

36. J. E. Schultz, J. Natarajan, Regulated unfolding: A basic principle of intraprotein signaling in modular proteins. *Trends Biochem. Sci.* **38**, 538–545 (2013).

37. H. N. Motlagh, J. O. Wrabl, J. Li, V. J. Hilser, The ensemble nature of allostery. *Nature* **508**, 331–339 (2014).

38. Y. Liu, H. K. Salter, A. N. Holding, C. M. Johnson, E. Stephens, P. J. Lukavsky, J. Walshaw, S. L. Bullock, Bicaudal-D uses a parallel, homodimeric coiled coil with heterotypic registry to coordinate recruitment of cargos to dynein. *Genes Dev.* **27**, 1233–1246 (2013).

39. R. Croasdale, F. J. Ivins, F. Muskett, T. Daviter, D. J. Scott, T. Hardy, S. J. Smerdon, A. M. Fry, M. Pfuhl, An undecided coiled coil: The leucine zipper of nek2 kinase exhibits atypical conformational exchange dynamics. *J. Biol. Chem.* **286**, 27537–27547 (2011).

40. M. Hulko, F. Berndt, M. Gruber, J. U. Linder, V. Truffault, A. Schultz, J. Martin, J. E. Schultz, A. N. Lupas, M. Coles, The HAMP domain structure implies helix rotation in transmembrane signaling. *Cell* **126**, 929–940 (2006).

41. C. M. Stewart, C. Z. Buffalo, J. A. Valderrama, A. Henningham, J. N. Cole, V. Nizet, P. Ghosh, Coiled-coil destabilizing residues in the group A *Streptococcus* M1 protein are required for functional interaction. *Proc. Natl. Acad. Sci. U.S.A.* **113**, 9515–9520 (2016).

42. H. N. Motlagh, V. J. Hilser, Agonism/antagonism switching in allosteric ensembles. *Proc. Natl. Acad. Sci. U.S.A.* **109**, 4134–4139 (2012).

43. J. Guo, H.-X. Zhou, Protein allostery and conformational dynamics. *Chem. Rev.* **116**, 6503–6515 (2016).

44. H. Liu, J. H. Naismith, An efficient one-step site-directed deletion, insertion, single and multiple-site plasmid mutagenesis protocol. *BMC Biotechnol.* **8**, 91 (2008).

45. G. D. Van Duyne, R. F. Standaert, P. A. Karplus, S. L. Schreiber, J. Clardy, Atomic structures of the human immunophilin FKBP-12 complexes with FK506 and rapamycin. *J. Mol. Biol.* **229**, 105–124 (1993).

46. F. Rao, Y. Yang, Y. Qi, Z.-X. Liang, Catalytic mechanism of cyclic di-GMP-specific phosphodiesterase: A study of the EAL domain-containing RocR from *Pseudomonas aeruginosa*. *J. Bacteriol.* **190**, 3622–3631 (2008).

47. D. Antoniani, P. Bocci, A. Maciag, N. Raffaelli, P. Landini, Monitoring of diguanylate cyclase activity and of cyclic-di-GMP biosynthesis by whole-cell assays suitable for high-throughput screening of biofilm inhibitors. *Appl. Microbiol. Biotechnol.* **85**, 1095–1104 (2010).

48. W. Kabsch, XDS. *Acta Crystallogr. D Biol. Crystallogr.* **D66**, 125–132 (2010).

49. P. D. Adams, P. V. Afonine, G. Bunkóczi, V. B. Chen, I. W. Davis, N. Echols, J. J. Headd, L.-W. Hung, G. J. Kapral, R. W. Grosse-Kunstleve, A. J. McCoy, N. W. Moriarty, R. Oeffner, R. J. Read, D. C. Richardson, J. S. Richardson, T. C. Terwilliger, P. H. Zwart, PHENIX: A comprehensive Python-based system for macromolecular structure solution. *Acta Crystallogr. D Biol. Crystallogr.* **D66**, 213–221 (2010).

50. G. Bunkóczi, R. J. Read, Improvement of molecular-replacement models with Sculptor. *Acta Crystallogr. D Biol. Crystallogr.* **D67**, 303–312 (2011).

51. A. J. McCoy, R. W. Grosse-Kunstleve, P. D. Adams, M. D. Winn, L. C. Storoni, R. J. Read, Phaser crystallographic software. *J. Appl. Cryst.* **40**, 658–674 (2007).

52. A. Winkler, T. R. M. Barends, A. Udvarhelyi, D. Lenherr-Frey, L. Lomb, A. Menzel, I. Schlichting, Structural details of light activation of the LOV2-based photoswitch PA-Rac1. *ACS Chem. Biol.* **10**, 502–509 (2015).

53. R. Lindner, X. Lou, J. Reinstein, R. L. Shoeman, F. A. Hamprecht, A. Winkler, Hexicon 2: Automated processing of hydrogen-deuterium exchange mass spectrometry data with improved deuteration distribution estimation. *J. Am. Soc. Mass Spectrom.* **25**, 1018–1028 (2014).

54. D. I. Svergun, Determination of the regularization parameter in indirect-transform methods using perceptual criteria. *J. Appl. Cryst.* **25**, 495–503 (1992).

55. A. Bergmann, G. Fritz, O. Glatter, Solving the generalized indirect Fourier transformation (GIFT) by Boltzmann simplex simulated annealing (BSSA). *J. Appl. Cryst.* **33**, 1212–1216 (2000).

56. D. Franke, D. I. Svergun, *DAMMIF*, a program for rapid ab-initio shape determination in small-angle scattering. *J. Appl. Cryst.* **42**, 342–346 (2009).

57. M. B. Kozin, D. I. Svergun, Automated matching of high- and low-resolution structural models. *J. Appl. Cryst.* **34**, 33–41 (2001).

58. M. V. Petoukhov, D. Franke, A. V. Shkumatov, G. Tria, A. G. Kikhney, M. Gajda, C. Gorba, H. D. T. Mertens, P. V. Konarev, D. I. Svergun, New developments in the *ATSAS* program package for small-angle scattering data analysis. *J. Appl. Cryst.* **45**, 342–350 (2012).

59. J. McGeehan, R. B. G. Ravelli, J. W. Murray, R. L. Owen, F. Cipriani, S. McSweeney, M. Weik, E. F. Garman, Colouring cryo-cooled crystals: Online microspectrophotometry. *J. Synchrotron Rad.* **16**, 163–172 (2009).

60. E. S. Burgie, A. N. Bussell, J. M. Walker, K. Dubiel, R. D. Vierstra, Crystal structure of the photosensing module from a red/far-red light-absorbing plant phytochrome. *Proc. Natl. Acad. Sci. U.S.A.* **111**, 10179–10184 (2014).

61. E. S. Burgie, T. Wang, A. N. Bussell, J. M. Walker, H. Li, R. D. Vierstra, Crystallographic and electron microscopic analyses of a bacterial phytochrome reveal local and global rearrangements during photoconversion. *J. Biol. Chem.* **289**, 24573–24587 (2014).

62. E. Krissinel, K. Henrick, Inference of macromolecular assemblies from crystalline state. *J. Mol. Biol.* **372**, 774–797 (2007).

63. M. Tarnawski, T. R. M. Barends, I. Schlichting, Structural analysis of an oxygen-regulated diguanylate cyclase. *Acta Crystallogr. D Biol. Crystallogr.* **D71**, 2158–2177 (2015).

64. A. M. Waterhouse, J. B. Procter, D. M. A. Martin, M. Clamp, G. J. Barton, Jalview Version 2—A multiple sequence alignment editor and analysis workbench. *Bioinformatics* **25**, 1189–1191 (2009).

65. H. Takala, H. Lehtivuori, H. Hammarén, V. P. Hytönen, J. A. Ihalainen, Connection between absorption properties and conformational changes in *Deinococcus radiodurans* phytochrome. *Biochemistry* **53**, 7076–7085 (2014).

66. D. Svergun, C. Barberato, M. H. J. Koch, CRYSOL—A program to evaluate x-ray solution scattering of biological macromolecules from atomic coordinates. *J. Appl. Cryst.* **28**, 768–773 (1995).

Citation: G. Gourinchas, S. Etzl, C. Göbl, U. Vide, T. Madl, A. Winkler, Long-range allosteric signaling in red light–regulated diguanylyl cyclases. *Sci. Adv.* **3**, e1602498 (2017).